remote sensing

MDPI

Article

Landscape Effects of Wildfire on Permafrost Distribution in Interior Alaska Derived from Remote Sensing

Dana R.N. Brown [1,2,*], Mark T. Jorgenson [3], Knut Kielland [1,2], David L. Verbyla [4], Anupma Prakash [5] and Joshua C. Koch [6]

1 Department of Biology and Wildlife, University of Alaska Fairbanks, Fairbanks, AK 99775, USA; kkielland@alaska.edu
2 Institute of Arctic Biology, University of Alaska Fairbanks, Fairbanks, AK 99775, USA
3 Alaska Ecoscience, Fairbanks, AK 99709, USA; ecoscience@alaska.net
4 Department of Natural Resources Management, University of Alaska Fairbanks, Fairbanks, AK 99775, USA; dlverbyla@alaska.edu
5 Geophysical Institute, University of Alaska Fairbanks, Fairbanks, AK 99775, USA; aprakash@alaska.edu
6 U.S. Geological Survey, Alaska Science Center, Anchorage, AK 99508, USA; jkoch@usgs.gov
* Correspondence: drnossov@alaska.edu; Tel.: +1-907-687-5707

Academic Editors: Ioannis Gitas, Randolph H. Wynne and Prasad S. Thenkabail
Received: 9 June 2016; Accepted: 9 August 2016; Published: 12 August 2016

Abstract: Climate change coupled with an intensifying wildfire regime is becoming an important driver of permafrost loss and ecosystem change in the northern boreal forest. There is a growing need to understand the effects of fire on the spatial distribution of permafrost and its associated ecological consequences. We focus on the effects of fire a decade after disturbance in a rocky upland landscape in the interior Alaskan boreal forest. Our main objectives were to (1) map near-surface permafrost distribution and drainage classes and (2) analyze the controls over landscape-scale patterns of post-fire permafrost degradation. Relationships among remote sensing variables and field-based data on soil properties (temperature, moisture, organic layer thickness) and vegetation (plant community composition) were analyzed using correlation, regression, and ordination analyses. The remote sensing data we considered included spectral indices from optical datasets (Landsat 7 Enhanced Thematic Mapper Plus (ETM+) and Landsat 8 Operational Land Imager (OLI)), the principal components of a time series of radar backscatter (Advanced Land Observing Satellite—Phased Array type L-band Synthetic Aperture Radar (ALOS-PALSAR)), and topographic variables from a Light Detection and Ranging (LiDAR)-derived digital elevation model (DEM). We found strong empirical relationships between the normalized difference infrared index (NDII) and post-fire vegetation, soil moisture, and soil temperature, enabling us to indirectly map permafrost status and drainage class using regression-based models. The thickness of the insulating surface organic layer after fire, a measure of burn severity, was an important control over the extent of permafrost degradation. According to our classifications, 90% of the area considered to have experienced high severity burn (using the difference normalized burn ratio (dNBR)) lacked permafrost after fire. Permafrost thaw, in turn, likely increased drainage and resulted in drier surface soils. Burn severity also influenced plant community composition, which was tightly linked to soil temperature and moisture. Overall, interactions between burn severity, topography, and vegetation appear to control the distribution of near-surface permafrost and associated drainage conditions after disturbance.

Keywords: wildfire; permafrost; remote sensing; boreal forest; Alaska

1. Introduction

Permafrost is vulnerable to thawing with continued climate warming, particularly in the boreal forest region where the mean annual permafrost temperature is close to 0 °C [1]. Permafrost degradation has begun in some areas, and widespread thawing over the next century is predicted under future climate scenarios [2,3]. The resilience of permafrost to climate change is enhanced where it is insulated by the accumulation of thick layers of organic material on the ground surface [4,5]. Conversely, the loss of this protective organic layer through wildfire combustion is a major positive feedback to permafrost degradation [6]. The thickness of the surface organic layer of soil remaining after fire, related to burn severity, is a critical control on the magnitude of permafrost degradation [6–8]. Fire is a widespread disturbance of the boreal forest, and the impacts of fire in Alaska appear to have recently intensified as a result of climate warming, with increased fire frequency, extent, and severity [9,10]. Climate change coupled with the intensifying wildfire regime is becoming a significant driver of permafrost loss and ecosystem change in the northern boreal forest [6–8,11].

Permafrost strongly influences ecosystem processes and hydrology, and plays a significant role in the global climate system by sequestering large quantities of carbon [12–14]. The thawing of permafrost allows for the release of carbon that was previously immobilized in frozen soils. Permafrost thawing can also cause changes in microtopography and drainage. The effects of thaw vary spatially depending upon factors such as soil texture, permafrost ice content, and topography [15]. For example, fine-textured soils with high ice content are likely to subside with thawing, potentially leading to surface water impoundment in flat, low-lying areas [8,16], or greater drainage and further permafrost erosion in upland areas [17]. Thawing in coarse-textured soils, and especially on slopes, is likely to cause increased drainage [18,19]. These contrasting effects of thawing can lead to either wetter or drier soil environments [20]. Loss of permafrost and change in soil moisture regimes influence the rates and pathways of biogeochemical cycling, which in turn impact nutrient availability to plants and carbon release to the atmosphere [12]. The degradation of permafrost therefore has local to global scale ecological impacts.

To understand and quantify the impacts of thaw, there is a need to spatially characterize permafrost distribution, particularly with respect to the growing influence of wildfire [2,21]. As a subsurface thermal condition of soil, however, permafrost is a challenge to detect remotely. Diverse approaches to indirectly map permafrost have been developed, including geophysical techniques using airborne electromagnetic (AEM) data [22], thermal modeling of ground temperatures using climate data and/or land surface temperatures [2,23–25], and statistical-empirical methods relating land cover, topography, and spectral indices to permafrost characteristics [26–28]. This study applies the latter approach of establishing empirical relationships of remote sensing data with permafrost conditions, specifically within a wildfire burn.

Our study area was in a rocky upland landscape in the interior Alaskan boreal forest, for which there is a paucity of post-fire permafrost information due to the difficulty of manually sampling permafrost in these soils. Yet this landscape type comprises approximately 30% of the boreal region of Alaska [29,30] and is likely to experience accelerated thawing after severe wildfire burns [11,18,31], resulting in reductions in soil moisture and changes to landscape hydrology [18,32]. The primary objectives of this study were to (1) map near-surface permafrost distribution and associated drainage conditions a decade after wildfire and (2) analyze mechanisms controlling landscape-scale patterns of post-fire permafrost degradation. We collected field-based data on soil properties (temperature, moisture, organic layer thickness) and vegetation (plant community composition) and analyzed relationships with remote sensing variables using correlation, regression, and ordination analyses. Remote sensing variables were derived from optical (Landsat 7 Enhanced Thematic Mapper Plus (ETM+) and Landsat 8 Operational Land Imager (OLI)), radar (Advanced Land Observing Satellite—Phased Array type L-band Synthetic Aperture Radar (ALOS-PALSAR), and topographic (Light Detection and Ranging (LiDAR)) datasets. We considered spectral indices (differenced normalized burn ratio (dNBR), normalized difference vegetation index (NDVI), and

normalized difference infrared index (NDII)), the principal components of a time series of synthetic aperture radar (SAR) polarized data, and numerous topographic metrics. Empirical relationships between remote sensing data and measured soil properties were then used to classify permafrost status and drainage conditions across the wildfire burn.

2. Materials and Methods

2.1. Study Area and Design

The ~100 km^2 study area is within the boundaries of the 2004 Boundary Fire in the Nome Creek portion of the White Mountains National Recreation Area in the Yukon-Tanana Uplands ecoregion of interior Alaska (Figure 1). The climate of this region is characterized by cold winters, warm summers, and low precipitation [33]. The vegetation mosaic of this region is strongly influenced by disturbance legacies (primarily wildfire) and topographic control of microclimate. Across the region, black spruce forests dominate colder sites, such as valley bottoms and north-facing slopes, and are typically underlain by permafrost. White spruce occurs on warmer sites, such as active floodplains and south-facing slopes. Deciduous forest (aspen, birch, and balsam poplar) also occurs on warmer sites, especially following disturbance. After a severe fire that exposes mineral soil, early successional vegetation is often dominated by colonizing species (e.g., *Marchantia polymorpha*, *Ceratodon purpureus*, *Chamerion angustifolium*, *Salix* spp., *Populus tremuloides*), whereas low-severity burns have a greater proportion of surviving and resprouting pre-fire vegetation (e.g., *Sphagnum* spp., *Eriophorum vaginatum*, *Rubus chamaemorus*, *Rhododendron tomentosum*) [34,35].

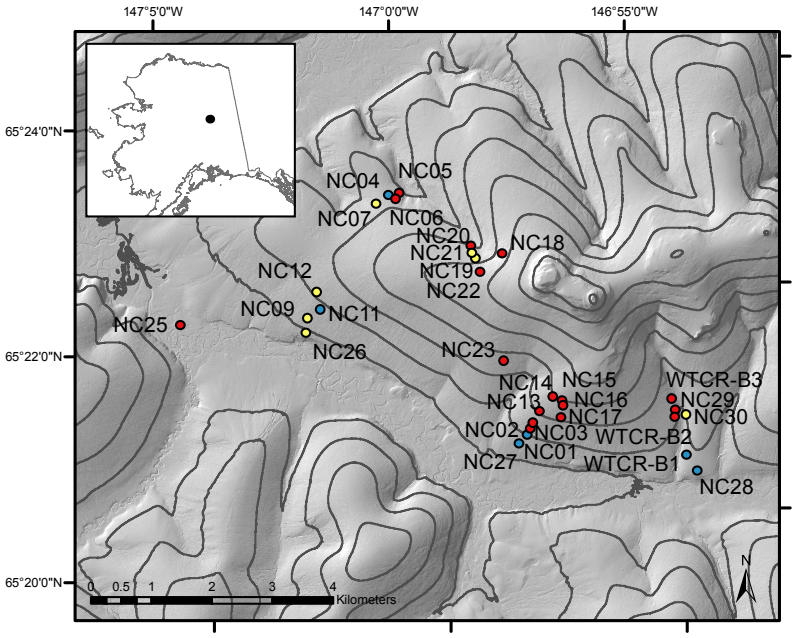

Figure 1. Map of study area and 30 field sites in the White Mountains National Recreation Area in interior Alaska. Symbols are colored to represent soil temperature at 1 m depth (blue: ≤0.00 °C; yellow: 0.01–2.00 °C; red: ≥2.01 °C). Contour lines (50-m) are overlain on a 2.5-m DEM.

In 2014, we established 30 field sites in burned black spruce stands, representing a range of topographic positions where we sampled vegetation and soils, and for which we extracted remote sensing data (Figure 1, Table 1). Field sites were located within patches of homogeneous land cover. Coordinates were obtained with a WAAS-enabled Garmin eTrex 30 GPS receiver with <3 m accuracy.

Within our study area, black spruce stands occurred in most landscape positions, including south-facing slopes. Our sites had relatively high elevations fairly close to the tree line. Five unburned patches of black spruce forest were also sampled, confirming the presence of near-surface permafrost

at these locations. Other studies in the study area have documented contrasting permafrost status between burned and unburned areas [18,36]. Permafrost was likely widespread but discontinuous in this study area before fire.

Table 1. Site-level environmental data (n = 30).

Site	Elevation (m)	Slope (°)	Organic Layer Thickness (cm)	Soil Temperature at 1 m (°C)	Soil Moisture (% vol.)	Vegetation Type
NC01	599	13	24	0.24	33	Low shrub
NC02	613	12	22	5.44	7	Low shrub
NC03	626	15	8	5.25	7	Low shrub
NC04	632	8	11	−0.04	30	Low shrub
NC05	617	20	8	4.77	23	Low shrub
NC06	633	13	13	3.43	16	Low shrub
NC07	633	12	9	1.01	34	Low shrub
NC09	565	9	13	0.74	53	Low shrub
NC11	588	10	14	−0.29	40	Low shrub
NC12	608	12	18	0.18	40	Low shrub
NC13	653	13	9	3.65	25	Low shrub
NC14	698	12	6	5.81	9	Bryoid herbaceous
NC15	700	11	15	3.57	7	Low shrub
NC16	690	13	12	6.65	28	Bryoid herbaceous
NC17	658	15	10	4.66	24	Low shrub
NC18	778	29	4	4.20	22	Grassy herbaceous
NC19	738	16	17	0.85	21	Low shrub
NC20	701	26	10	5.11	18	Low shrub
NC21	724	16	24	0.33	51	Low shrub
NC22	776	16	7	4.20	22	Bryoid herbaceous
NC24	680	14	11	5.68	30	Bryoid herbaceous
NC25	506	2	7	4.09	26	Low shrub
NC26	544	9	12	0.28	52	Low shrub
NC27	579	11	14	−0.22	65	Shrub-tussock
NC28	584	8	26	−0.24	42	Shrub-tussock
NC29	609	13	13	2.53	31	Low shrub
NC30	601	16	8	0.12	36	Low shrub
WTCR-B1	590	9	25	−0.17	48	Shrub-tussock
WTCR-B2	606	13	12	4.14	11	Low shrub
WTCR-B3	619	14	15	4.40	16	Low shrub

2.2. Vegetation Sampling

At each site we described plant species composition in detail and classified vegetation type following the methodology of Viereck [37]. Percent cover of each plant species was determined within a 10 × 5 m^2 area using either visual estimates or point-sampling, when time allowed. For visual estimates, a Braun–Blanquet cover class was assigned to each species [38]. For point-sampling, we recorded each species occurrence along a 100-point grid. Species present in the sampling area, but not encountered in point-sampling, were given a trace cover value of 0.1%. For consistency in analysis, percent cover values derived from point-sampling were converted to Braun–Blanquet cover classes. If plant species was uncertain, taxa were aggregated to the genus level for analysis.

2.3. Soil Sampling

Soils were sampled to determine stratigraphy, surface soil moisture, and presence of shallow permafrost. Soil moisture, temperature, and thaw depths were determined during a precipitation-free period, 11–13 September 2014. Descriptions of soil stratigraphy to ~40 cm depth were conducted for 2–3 soil plugs per site. Surface organic layer thickness (OLT) was considered a proxy for burn severity for analysis of field-based data. OLT was measured at 1-m intervals along the 10-m transect at each site. Volumetric water content of the upper 20 cm of the soil profile was also measured at 1-m intervals using a Campbell Scientific Hydrosense sensor. An additional dataset of soil moisture from a severely burned location was used to assess temporal patterns of soil moisture in relation to remote

sensing indices. Soil moisture at 7 cm depth was measured at 15-min intervals using moisture sensors (M005, Onset Computer Corporation, Fort Collins, CO, USA) attached to a data logger (H21-002, Onset Computer Corporation, Fort Collins, CO, USA). Data from the snow-free seasons of 2014 and 2015 were used in this analysis.

Permafrost presence, usually identified through mechanical probing with a metal rod, was difficult to determine at most of our sites due to the rocky soils. Instead, soil temperature at 1 m depth was used as an indicator of near-surface (1 m) permafrost presence. If soil temperature was above 0 °C at 1 m depth, shallow permafrost at this depth was considered absent, although permafrost may be present at greater depths. One to three boreholes were drilled to ~1 m depth at each site in the summer in preparation for soil temperature determination in fall, the time of maximum seasonal thaw. A 1.3 cm diameter drill bit was used with a portable Bosch Litheon hammer drill. The full length of each borehole was plugged with hollow polyethylene (PEX) tubing sealed at both ends with silicon and epoxy to prevent water pooling. Sites were revisited in the fall for temperature determination. The upper seal of the tubes were cut, thermistor sensors were slowly lowered to two depths (50 cm and the bottom depth), and temperatures were recorded after equilibration using an Omega HH41 thermistor thermometer.

If the bottom depth was not exactly 100 cm, we used the temperature gradient from 50 cm to the bottom depth to estimate the temperature at 1 m. Borehole depths ranged from 80 to 120 cm, so the maximum extrapolation of temperatures was 20 cm beyond the deepest temperature measurement. The temperature gradients were similar across most boreholes (n = 50), ranging from −0.035 to −0.003 °C/cm, with a mean of −0.013 °C/cm (SE = 0.001). At the three boreholes where thaw depth could be determined by frost probing, it was used to validate the gradients used to estimate 1 m temperatures, whereby the depth of 0 °C along the temperature gradient should approximate the measured thaw depth. Our predicted thaw depths deviated from measured thaw depths by 1 to 6 cm (mean = 3.7 cm).

2.4. Remote Sensing

The remote sensing involved use of a digital elevation model (DEM) derived from airborne Light Detection and Ranging (LiDAR) for topographic metrics, Landsat optical imagery, and synthetic aperture radar (SAR) (Tables 2 and 3). The details of imagery acquisition and processing are described below.

Table 2. Satellite remote sensing scenes used in analysis.

Satellite/Sensor	Date	Frame	Path
ALOS-PALSAR	8 August 2009	1300	253
ALOS-PALSAR	23 September 2009	1300	253
ALOS-PALSAR	11 August 2010	1300	253
ALOS-PALSAR	26 September 2010	1300	253
	Date	**Path**	**Row**
Landsat 8 OLI	2 June 2013	69	14
Landsat 8 OLI	18 June 2013	69	14
Landsat 8 OLI	13 July 2013	68	14
Landsat 8 OLI	12 August 2013	70	14
Landsat 8 OLI	15 September 2013	68	14
Landsat 8 OLI	20 May 2014	69	14
Landsat 8 OLI	30 July 2014	70	14
Landsat 8 OLI	24 August 2014	69	14
Landsat 8 OLI	9 September 2014	69	14
Landsat 8 OLI	18 September 2014	68	14
Landsat 8 OLI	23 May 2015	69	14
Landsat 8 OLI	15 June 2015	70	14
Landsat 8 OLI	4 August 2015	68	14
Landsat 8 OLI	3 September 2015	70	14
Landsat 7 ETM+	27 May 2002	69	14
Landsat 7 ETM+	22 July 2005	69	14

Table 3. Remote sensing variables used in analysis.

Variable	Source
Topographic	
Aspect	LiDAR DEM
CTI	LiDAR DEM
Curvature	LiDAR DEM
Elevation	LiDAR DEM
Slope	LiDAR DEM
Solar radiation	LiDAR DEM
Radar	
HH-PC1	ALOS-PALSAR
HH-PC2	ALOS-PALSAR
HH-PC3	ALOS-PALSAR
HH-PC4	ALOS-PALSAR
HV-PC1	ALOS-PALSAR
HV-PC2	ALOS-PALSAR
HV-PC3	ALOS-PALSAR
HV-PC4	ALOS-PALSAR
Optical	
dNBR	Landsat 7 ETM+
NDII6	Landsat 8 OLI
NDII7	Landsat 8 OLI
NDVI	Landsat 8 OLI

2.4.1. LiDAR

Topographic variables were extracted from a high-resolution DEM derived from airborne LiDAR. The LiDAR dataset was collected in 2010 with an ALTM Gemini system (Optech, Vaughan, Canada) operated by Aero-Metric, Inc. The horizontal accuracy was 1.05 m and vertical accuracy was 0.067 m. The raw data were processed by Aero-Metric, Inc. to produce a 2.5-m resolution DEM. From this DEM we extracted or computed the following topographic metrics: elevation, aspect, slope, curvature, direct solar radiation [39], and compound topographic index (CTI), a steady state wetness index based on catchment area and slope [40] (Table 3). Bilinear interpolation was used for extraction of topographic indices at site locations.

2.4.2. Radar

Microwave remote sensing has been successful in mapping soil moisture in burned boreal forest due to the sensitivity of radar backscatter to variation in soil moisture throughout the growing season [41,42]. In this study, we used L-band synthetic aperture radar (SAR) data from ALOS-PALSAR in fine beam dual polarization mode (Table 2). The polarizations used were horizontal transmit and horizontal receive (HH) and horizontal transmit and vertical receive (HV). Radiometric and terrain corrected (RTC) products (20-m resolution) were processed by the Alaska Satellite Facility. Because backscatter is influenced by topography, surface roughness, and vegetation cover, multi-temporal observations (August 2009, September 2009, August 2010, September 2010) were used to isolate the soil moisture signal. This approach assumes that moisture is the major time-variant factor within a season, and other influences on backscatter are somewhat constant, an assumption which appears to be valid in boreal forests after fire [41]. Backscatter data were extracted for each site location and converted to decibels. A principal components analysis (PCA) was conducted for the time series of HH and HV polarized data (Table 3).

2.4.3. Landsat

Several spectral indices were derived from Landsat 7 ETM+ and Landsat 8 OLI imagery (Tables 2 and 3). The differenced normalized burn ratio (dNBR) was used as a remote sensing indicator of burn severity. We used a dNBR product (ID: BLM-AKAFS-A4SZ-20040613) acquired from the Monitoring Trends in Burn Severity (MTBS) program of the U.S. Geological Survey and U.S. Forest Service. The dNBR dataset from the MTBS program was originally derived from Landsat 7 ETM+ imagery acquired before and after fire. The normalized burn ratio (NBR) of pre-fire and post-fire imagery was calculated using the red, near infrared (NIR), and shortwave infrared (SWIR) bands as follows:

$$\mathrm{NBR} = (\mathrm{NIR} - \mathrm{SWIR})/(\mathrm{NIR} + \mathrm{SWIR}) \quad (1)$$

where NIR is band 4 (0.77–0.90 μm) and SWIR is band 7 (2.09–2.35 μm). dNBR is the difference between pre-fire and post-fire NBR:

$$\mathrm{dNBR} = \mathrm{pre-fire\,NBR} - \mathrm{post-fire\,NBR} \quad (2)$$

We used the dNBR index for correlations with soil and vegetation properties, and used the thematic map to exclude unburned areas from our mapping and to differentiate levels of burn severity (low, moderate, and high).

The normalized difference vegetation index (NDVI) and normalized difference infrared index (NDII) were computed as follows using the red, NIR, and SWIR bands of the Landsat 8 OLI sensor:

$$\mathrm{NDVI} = (\mathrm{NIR} - \mathrm{red})/(\mathrm{NIR} + \mathrm{red}) \quad (3)$$

$$\mathrm{NDII} = (\mathrm{NIR} - \mathrm{SWIR})/(\mathrm{NIR} + \mathrm{SWIR}) \quad (4)$$

where red is band 4 (0.64–0.67 μm) and NIR is band 5 (0.85–0.88 μm). NDII6 was calculated using SWIR1 band 6 (1.57–1.65 μm), and NDII7 was calculated using SWIR2 band 7 (2.11–2.29 μm). The nomenclature for NDII6 and NDII7 identifies the SWIR OLI band used. We extracted surface reflectance values for each site location and calculated spectral indices using Landsat 8 OLI Surface Reflectance products (30-m resolution) processed by the U.S. Geological Survey. The processing of Landsat 8 OLI Surface Reflectance products included the application of a physically-based atmospheric correction algorithm, the Landsat Surface Reflectance Code (LaSRC), which uses the narrow OLI coastal aerosol band (0.433–0.450 μm) for aerosol inversion tests, ancillary climate data from Moderate Resolution Imaging Spectroradiometer (MODIS), and radiative transfer models [43,44]. The scene used for correlation analyses with ground-based data and for mapping was acquired on 9 September 2014, within four days of field soil sampling. Analysis of temporal variation in surface reflectance relative to plant phenology and soil moisture was conducted using 14 additional scenes from the snow-free seasons of 2013–2015.

2.5. Data Analysis

2.5.1. Vegetation

Analysis of plant communities and relationships with environmental and remote sensing variables were conducted using nonmetric multidimensional scaling (NMDS) (PC-ORD 6, MjM Software, 2011). This multivariate ordination technique extracts the dominant patterns of plant species composition across sites into two continuous synthetic variables represented by the ordination axes [45]. In the ordination diagram, each point represents the plant community composition at a site. The distance between points represents the dissimilarity between plant communities. Relationships between plant communities (NMDS ordination axis scores) and environmental and remote sensing variables were examined with correlation analyses. The strength and direction of these relationships are depicted by vectors in the ordination diagram.

2.5.2. Soils

Statistical analyses were conducted using JMP Pro 11 (SAS Institute, Inc., Cary, NC, USA, 2013). The distributions of field data were assessed for normality using the Shapiro–Wilk test. Soil temperature at 1 m depth exhibited a non-normal bimodal distribution ($W = 0.87$, $p < W = 0.0018$), precluding parametric statistical analyses. Sites were grouped into "cold" and "warm" classes based on the bimodal soil temperature distribution. The cold soil class was defined by temperatures ≤ 1.0 °C ($n = 13$) and the warm soil class had temperatures ≥ 2.5 °C ($n = 17$). Relationships among variables were assessed using a combination of nonparametric correlation analyses (Spearman's rank), *t*-tests among soil temperature classes, and regression analyses when statistical assumptions were met. Results were considered statistically significant where $p < 0.05$.

2.5.3. Remote Sensing

Relationships between numerous remote sensing variables (Table 3) and soil moisture, and temperature, and organic layer thickness were tested using nonparametric correlation analyses (Spearman's rank) due to the non-normal distribution of data. The strongest indicator of subsurface properties, NDII7, was then used in mapping. To better understand the extent to which vegetation and/or soil properties were driving the observed NDII7 response, we conducted analyses of the seasonal patterns of NDII7 and its components (NIR and SWIR reflectance) at our field sites in relation to plant phenology and soil moisture from May through September of 2013, 2014, and 2015 for warm and cold soil temperature classes. We also analyzed variation in soil moisture (7 cm depth) over time at a monitoring site in a severely burned area in relation to reflectance.

2.5.4. Mapping

The empirical relationships between NDII7, soil moisture, and soil temperature from September 2014 were used to map drainage conditions and permafrost distribution in our study area a decade after fire. The linear relationship between NDII7 and surface soil moisture (upper 20 cm) was applied to each 30-m pixel in the study area to estimate volumetric water content of soils. The pixels were grouped into soil moisture classes based on volumetric water content using the Jenks optimization method [46]. The moisture classes were characterized as well drained, moderately drained, or poorly drained. Because soil water content fluctuates temporally and this map is based on single-date measurements, it is intended to represent relative drainage conditions rather than absolute water content. For the permafrost map, thresholds of NDII7 values were used to divide soil temperature predictions into three classes (present, absent, unknown) that reflect the probability of near-surface (~1 m) permafrost presence. Sample size precluded an accuracy assessment of the map. Unburned areas, as determined by dNBR, were excluded from thematic maps. These maps were used to analyze the spatial extent and distribution of drainage and permafrost classes across the landscape and in relation to the remote sensing burn severity indicator (dNBR).

3. Results

3.1. Vegetation

The vegetation structure of the majority (73%) of our sites consisted of low shrub communities dominated by *Rhododendron tomentosum*, *Vaccinium uliginosum*, or *Betula glandulosa* (Table 1). Thirteen percent of the sites were bryoid herbaceous meadows that had a mix of shrubs, forbs, graminoids, and mosses, but had the greatest cover of mosses *Ceratodon purpureus* and *Polytrichum juniperinum*. Ten percent of the sites were shrub-tussock meadows dominated by *Eriophorum vaginatum* and *Rhododendron tomentosum*. One outlier graminoid herbaceous site dominated by grasses (*Calamagrostis canadensis*) was excluded from the NMDS analysis.

The NMDS diagrams show the variation in plant community composition across sites, with vector length and direction indicating the relationships with vegetation, environmental, and remote

sensing variables (Figure 2). Sites with similar vegetation structure were grouped closely together, with shrub-tussock meadows and bryoid herbaceous meadows each clustered on opposing extremes of Axis 1 (Figure 2A). Axis 1 was negatively correlated with sedge tussock ($r = -0.62$), low shrub ($r = -0.63$), and dwarf shrub cover ($r = -0.55$); and was positively correlated with grass cover ($r = 0.66$) (Figure 2A, Table 4). Cover of other growth forms (evergreen tree, deciduous tree, tall shrub, moss, forbs, sedges, lichens) were not associated with either axis.

Numerous individual species/genera were associated with the ordination axes (Figure 2B, Table 4). The strongest correlations were related to Axis 1: *Rubus chamaemorus* ($r = -0.72$), *Ceratodon purpureus* ($r = 0.69$), *Rhododendron* spp. ($r = -0.69$), *Eriophorum vaginatum* ($r = -0.62$), *Cornus canadensis* ($r = 0.60$), and *Sphagnum* spp. ($r = -0.58$) (Figure 2B, Table 4). The strongest correlations with Axis 2 were *Chamerion angustifolium* ($r = 0.56$), *Alnus viridis* ssp. *crispa* ($r = -0.52$), *Rosa acicularis* ($r = 0.49$), and *Vaccinium uliginosum* ($r = 0.49$).

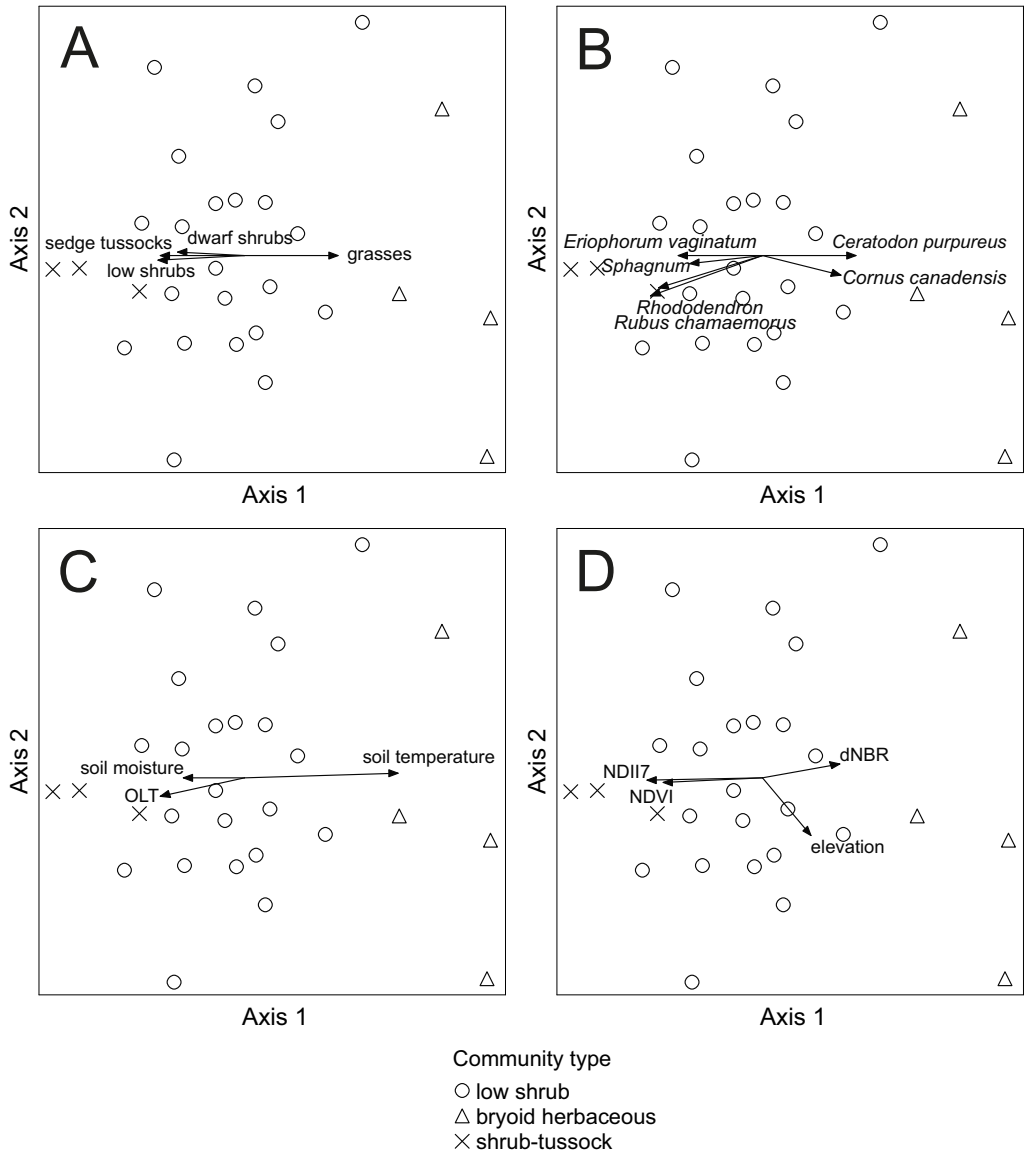

Figure 2. NMDS ordination of plant communities and relationships with (**A**) vegetation cover by growth form; (**B**) vegetation cover by species or genus; (**C**) soil properties; and (**D**) remote sensing variables. One outlier was excluded ($n = 29$). Each point represents the plant community composition at a site. The vectors show the strength and direction of correlations.

Table 4. Pearson and Kendall correlations of NMDS ordination axes with vegetation cover (by type and species), soil properties, and remote sensing metrics. Variables correlated with at least one axis with $R^2 > 0.2$ are shown with coefficients of determination are highlighted in bold. One outlier was excluded ($n = 29$).

		Axis 1			Axis 2		
		r	***R²***	***tau***	***r***	***R²***	***tau***
	Vegetation type (% cover)						
	Dwarf shrubs	−0.55	**0.31**	−0.37	0.12	0.01	0.05
	Low shrubs	−0.63	**0.39**	−0.40	−0.14	0.02	−0.04
	Grasses	0.66	**0.43**	0.51	0.05	0.00	−0.07
	Plant species (% cover)						
Tall shrubs	*Alnus incana* ssp. *crispa*	0.22	0.05	0.08	−0.52	**0.27**	−0.37
Low shrubs	*Rhododendron* spp.	−0.69	**0.47**	−0.46	−0.38	0.15	−0.28
	Rosa acicularis	0.40	0.16	0.30	0.49	**0.24**	0.34
	Vaccinium uliginosum	−0.53	**0.28**	−0.37	0.49	**0.24**	0.43
Dwarf shrubs	*Vaccinium vitis-idaea*	−0.51	**0.26**	−0.43	0.12	0.02	0.11
Forbs	*Aster sibirica*	0.55	**0.30**	0.34	−0.07	0.01	−0.03
	Cornus canadensis	0.60	**0.36**	0.47	−0.30	0.09	−0.35
	Chamerion angustifolium	0.46	**0.21**	0.40	0.56	**0.31**	0.44
	Rubus chamaemorus	−0.72	**0.52**	−0.59	−0.43	0.19	−0.30
Sedges	*Carex bigelowii*	0.53	**0.28**	0.48	−0.18	0.03	−0.20
Sedge tussocks	*Eriophorum vaginatum*	−0.62	**0.39**	−0.68	0.02	0.00	0.19
Mosses	*Ceratodon purpureus*	0.69	**0.48**	0.45	−0.07	0.01	0.05
	Polytrichum juniperinum	0.47	**0.22**	0.43	0.01	0.00	−0.19
	Sphagnum spp.	−0.58	**0.33**	−0.55	−0.19	0.04	−0.21
	Soil properties						
	OLT	**−0.62**	**0.38**	**−0.49**	−0.15	0.02	−0.01
	Soil moisture, 20 cm	**−0.53**	**0.28**	**−0.43**	0.22	0.05	0.22
	Soil temperature, 1 m	**0.84**	**0.71**	**0.69**	0.03	0.00	−0.03
	Remote sensing variables						
	Elevation	0.44	0.19	0.35	**−0.62**	**0.38**	**−0.45**
	NDII7	**−0.73**	**0.54**	**−0.57**	0.02	0.00	0.03
	NDVI	**−0.68**	**0.46**	**−0.42**	−0.04	0.00	−0.03
	dNBR	**0.60**	**0.35**	**0.52**	0.02	0.00	0.03

3.2. Soils

There were strong relationships among surface organic layer thickness (OLT), soil temperature, and moisture after the 2004 fire (Table 4). OLT was inversely related to soil temperature at 1 m depth (Figure 3A, $n = 30$, Spearman's $\rho = -0.51$, $p = 0.004$). A strong inverse relationship between soil temperature at 1 m depth and surface soil moisture of the upper 20 cm was found across our sites (Figure 3B, $n = 30$, Spearman's $\rho = -0.71$, $p < 0.0001$). The warm soil class ($\geq$2.5 °C) had a lower mean OLT (10.6 cm vs. 16.5 cm) and volumetric soil moisture (19.0% vs. 41.9%) than the cold soil class ($\leq$1.0 °C) (Figure 4). These soil properties were also related to the NMDS ordination of plant communities (Figure 2C, Table 4). NMDS Axis 1 had a strong positive correlation with soil temperature ($r = 0.84$) and a negative correlation with soil moisture ($r = -0.53$) and OLT ($r = -0.62$).

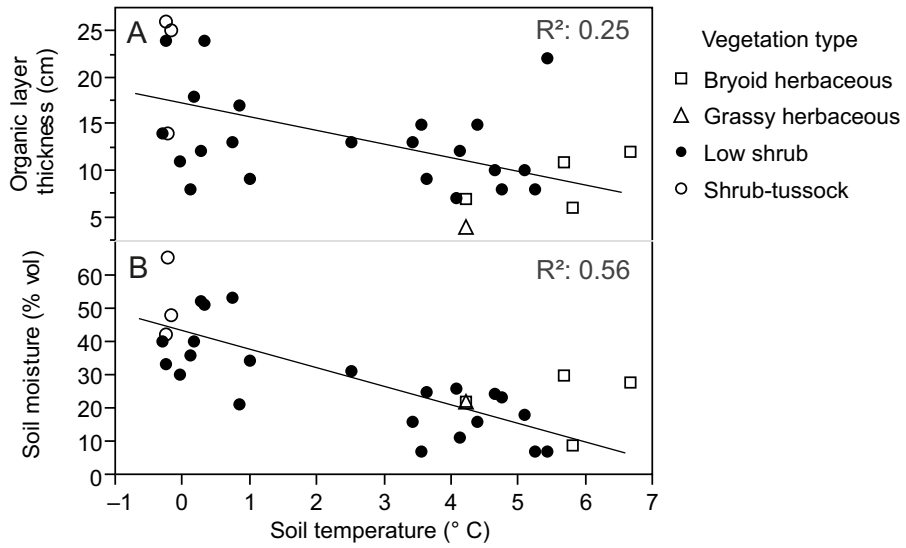

Figure 3. Relationships between soil temperature (1 m depth) and (**A**) organic layer thickness and (**B**) surface soil moisture (upper 20 cm), by vegetation type (n = 30).

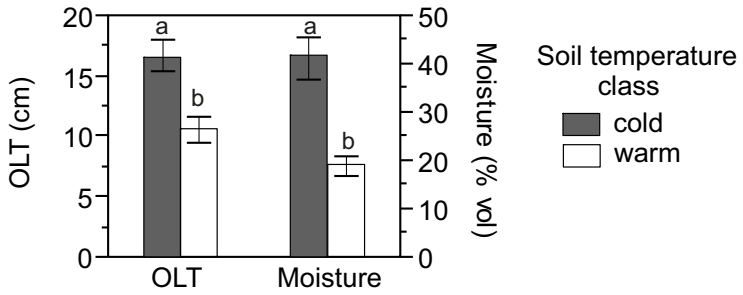

Figure 4. Mean ± SE organic layer thickness (OLT) and soil moisture by soil temperature class. Significant differences between cold (≤1.0 °C, n = 13) and warm (≥2.5 °C, n = 17) groups were determined with two-tailed t-tests and denoted by lettering.

3.3. Remote Sensing

Topographic variables derived from the DEM were related to soil moisture and temperature, but not significantly related to organic layer thickness (Table 5). Elevation and slope were significantly correlated with both moisture ($\rho = -0.53$, $p = 0.0025$; $\rho = -0.38$, $p = 0.0395$; respectively) and temperature (ρ = 0.54, p = 0.0023; ρ = 0.48, p = 0.0078; respectively). No significant correlations were found for aspect, CTI, curvature, or solar radiation. Of the topographic variables, only elevation was associated with the plant community ordination (Figure 2D, Table 4). Elevation had a negative correlation with NMDS Axis 2 ($r = -0.62$) and a positive correlation with Axis 1 (r = 0.47).

From the SAR dataset, the first principal component of the HV polarization time series was significantly correlated with soil moisture (ρ = 0.42, p = 0.0200), but only weakly correlated with soil temperature ($\rho = -0.36$, p = 0.0516), and organic layer thickness (ρ = 0.35, p = 0.0580) (Table 5). No additional relationships were found between soil properties and other principal components of the HH or HV polarizations. The SAR-derived variables were not associated with either axis of the plant community ordination.

Landsat-derived indices, particularly those within the infrared region, showed strong relationships with soil properties and vegetation (Tables 4 and 5, Figure 2D). dNBR was negatively correlated with soil moisture ($\rho = -0.53$; p = 0.0026), positively correlated with temperature (ρ = 0.64, p = 0.0001), though only weakly correlated with organic layer thickness ($\rho = -0.29$; p = 0.1201).

NDVI was positively associated with soil moisture (ρ = 0.39, p = 0.0345), and negatively associated with soil temperature (ρ = −0.57, p = 0.0009). The infrared indices (NDII6 and NDII7) were the remote sensing metrics most highly correlated with measured soil properties. NDII7, in particular, emerged as the best predictor of surface soil moisture (ρ = 0.69, $p < 0.0001$), soil temperature (ρ = −0.83, $p < 0.0001$) at depth, and organic layer thickness (ρ = −0.36, p = 0.0456). All of the infrared remote sensing indices that were correlated with soil properties were also correlated with the plant community ordination axes. NMDS Axis 1 was negatively correlated with NDII7 (r = −0.73) and NDVI (r = −0.67), and positively correlated with dNBR (r = 0.60). Based on the strength of the correlations, NDII7 was chosen for regression-based spatial modeling of soil properties and more detailed analyses of relationships with soils and vegetation.

Table 5. Spearman's rank correlations (ρ) between remote sensing metrics, volumetric soil moisture (upper 20 cm), soil temperature (1 m), and surface organic layer thickness. Significant relationships are highlighted in bold (n = 30).

Remote Sensing Dataset	Variable	Soil Moisture		Soil Temperature		Organic Layer Thickness	
		ρ	*Prob* > |ρ|	ρ	*Prob* > |ρ|	ρ	*Prob* > |ρ|
Topographic	Aspect	0.21	0.2638	−0.12	0.5271	−0.33	0.0780
	CTI	−0.15	0.4409	0.08	0.6611	−0.01	0.9805
	Curvature	0.22	0.2476	−0.04	0.8336	−0.03	0.8767
	Elevation	**−0.53**	**0.0025**	**0.54**	**0.0023**	−0.28	0.1275
	Slope	**−0.38**	**0.0395**	**0.48**	**0.0078**	−0.31	0.0961
	Solar radiation	−0.07	0.7042	0.20	0.2975	0.13	0.5020
Radar	HH-PC1	−0.21	0.2764	−0.03	0.8923	−0.03	0.8840
	HH-PC2	0.08	0.6697	0.02	0.9015	−0.03	0.8656
	HH-PC3	0.29	0.1251	−0.29	0.1234	0.02	0.9025
	HH-PC4	0.07	0.7042	−0.10	0.6084	−0.02	0.9006
	HV-PC1	**0.42**	**0.0200**	−0.36	0.0516	0.35	0.0580
	HV-PC2	0.12	0.5419	−0.03	0.8573	0.14	0.4651
	HV-PC3	0.22	0.2486	−0.03	0.8812	−0.17	0.3597
	HV-PC4	−0.07	0.7164	−0.08	0.6894	−0.08	0.6680
Optical	dNBR	**−0.53**	**0.0026**	**0.64**	**0.0001**	−0.29	0.1201
	NDII6	**0.66**	**<0.0001**	**−0.81**	**<0.0001**	0.32	0.0874
	NDII7	**0.69**	**<0.0001**	**−0.83**	**<0.0001**	**0.37**	**0.0456**
	NDVI	**0.39**	**0.0345**	**−0.57**	**0.0009**	0.35	0.0573

Sites from both soil temperature classes exhibited similar seasonal reflectance patterns, though the cold sites had higher NDII7 values, higher NIR reflectance, and lower SWIR reflectance (Figure 5). The seasonal reflectance patterns were generally consistent during 2013–2015. SWIR reflectance typically decreased from springtime through the summer, and slightly increased in fall. NDII7 and NIR reflectance both increased from springtime to mid–late summer and decreased in fall. An additional dataset of surface soil moisture from a severely burned site was used to assess temporal patterns of moisture in relation to spectral reflectance. Variation in surface soil moisture (at 7 cm depth) had a strong negative relationship with SWIR reflectance, and to a lesser extent with NDII7, and no significant relationship to NIR reflectance (Figure 6).

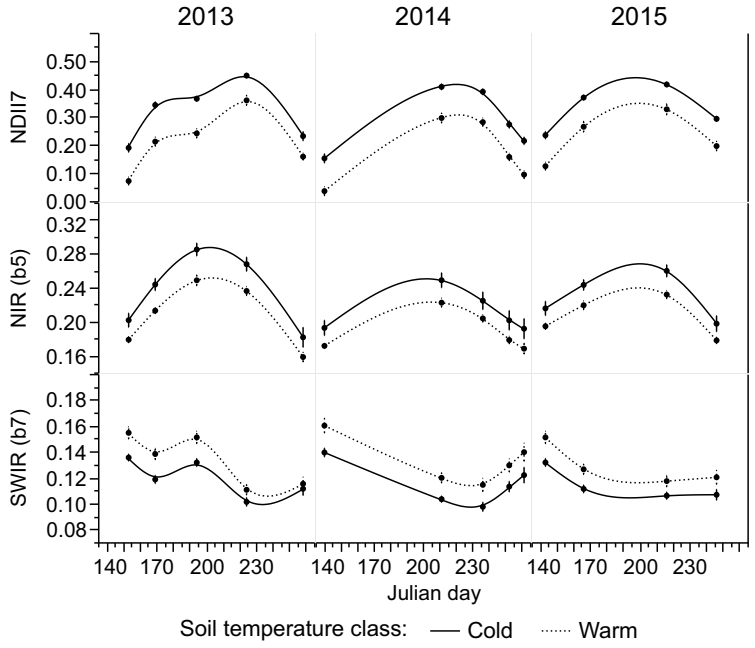

Figure 5. Seasonal patterns of NDII7, NIR, and SWIR reflectance (Landsat 8 OLI) from May–September of 2013–2015. Points represent means ± SE for field sites in cold (≤1.0 °C, n = 13) and warm (≥2.5 °C, n = 17) soil temperature classes.

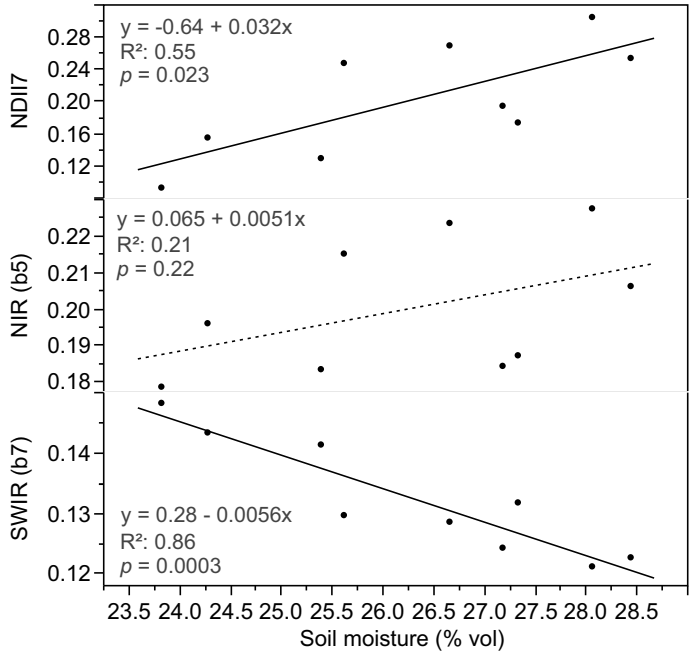

Figure 6. Relationships of NDII7, NIR, and SWIR reflectance (Landsat 8 OLI) with percent soil moisture (7 cm depth) at a field monitoring site in a severe burn. Each data point is from a different day in the 2014–2015 snow-free seasons (n = 9). Solid lines depict significant regressions; dashed lines depict insignificant regressions.

3.4. Mapping

The linear relationship between NDII7 and surface soil moisture (upper 20 cm) was used to map volumetric soil moisture content (Figure 7A). The pixels were grouped into six soil moisture classes using the Jenks optimization method (Figure 8A).

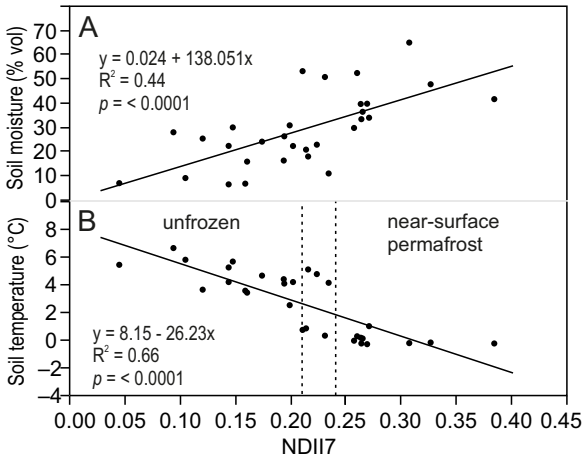

Figure 7. Relationships between NDII7 (Landsat 8 OLI) and (**A**) soil moisture (upper 20 cm); and (**B**) soil temperature (1 m) at field sites (n = 30). Vertical dashed lines represent cut-points used to delineate unfrozen from near-surface permafrost classes in mapping. All sites with NDII7 values < 0.21 had soil temperature ≥2.5 are were likely permafrost-free, whereas most sites with NDII7 values > 0.24 had soil temperatures near or below freezing, suggesting the presence of near-surface permafrost.

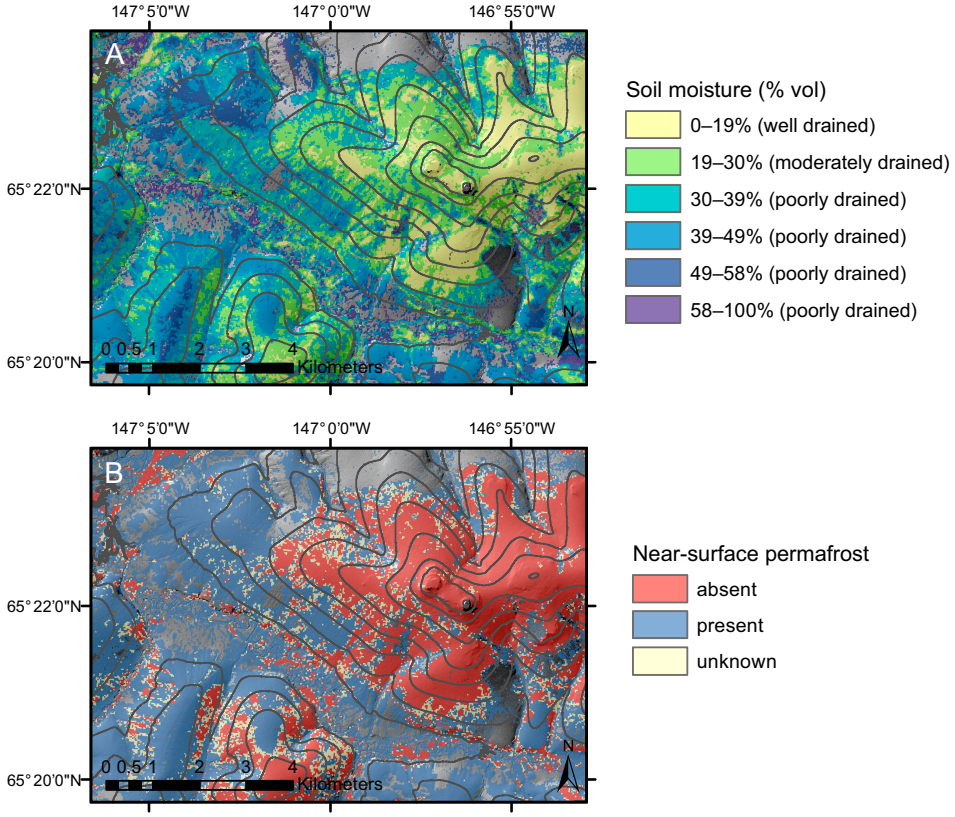

Figure 8. Maps of (**A**) soil moisture (% vol) of upper 20 cm and (**B**) near-surface permafrost (~1 m) distribution a decade after the 2004 Boundary Fire in interior Alaska with 50-m contour lines overlain on a DEM. Thematic maps are based on NDII7 calculations from a Landsat 8 OLI scene acquired 9 September 2014. Unburned areas are excluded.

The majority of the burned portion of the study area was classified as poorly drained (61%), 24% was considered moderately drained, and 15% was well drained (Figure 9A). Well drained and moderately drained classes were located primarily on ridgetops and upper hill slopes; whereas poorly

drained classes occurred mainly on lower lying areas, in concave drainage areas, and along linear water tracks (Figure 8A). There were exceptions to this overall pattern, with poorly drained areas occurring on hilltops and well-drained areas on lower hillslopes.

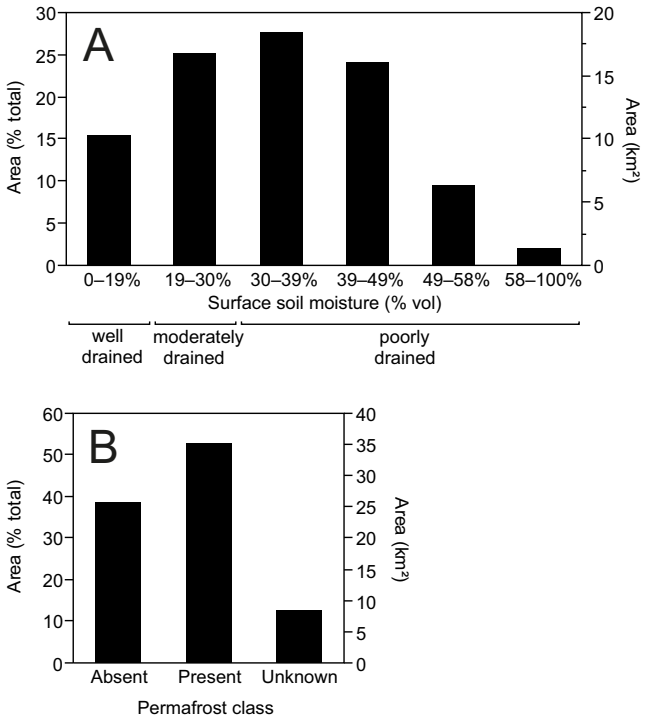

Figure 9. Distribution of mapped (**A**) drainage and (**B**) permafrost classes.

The permafrost map was produced using thresholds of NDII7 values, which were indicative of soil temperatures at 1 m depth (Figure 7B). At NDII7 values <0.21, 100% of sites had soil temperatures greater than 2.5 °C; therefore, with high certainty, this class was designated as unfrozen. Although permafrost is not expected within the upper meter in this class, permafrost may be present at greater depths. At NDII7 values >0.24, 89% of sites had soil temperatures between −0.3 and 0.3 °C; therefore, this class was considered to have a high probability of permafrost near 1 m depth. At intermediate NDII7 values, soil temperatures ranged from 0.3 to 5.1 °C, with half the sites having temperatures >4 °C and half having temperatures <0.5 °C. This group likely includes a mixture of permafrost conditions at 1 m depth, and therefore was classified as unknown permafrost status.

According to our mapping classifications, 51% of the study area was underlain by near-surface permafrost (within 1 m depth), 37% lacked permafrost, and 12% had unknown permafrost status (Figure 9B). Near-surface permafrost was distributed mainly on lower hillslopes, but also was found on hilltops and upper slopes (Figure 8B). Conversely, areas without near-surface permafrost occurred mainly on hilltops and upper slopes, but also on lower hillslopes. Areas of unknown permafrost status usually occurred on the boundaries between the areas with permafrost and without permafrost.

Permafrost status was related to burn severity class, as delineated by dNBR (Figure 10). 79% of the low burn severity area was underlain by near-surface permafrost according to our classification. 89% of the high burn severity area was classified as lacking near-surface permafrost. The moderate burn severity area had a relatively even mixture of permafrost classes (46% absent; 37% present). The moderate burn severity class also had the highest area of unknown permafrost status, suggesting that NDII7 performed better at differentiating permafrost status at both extremes of burn severity levels rather than at intermediate levels.

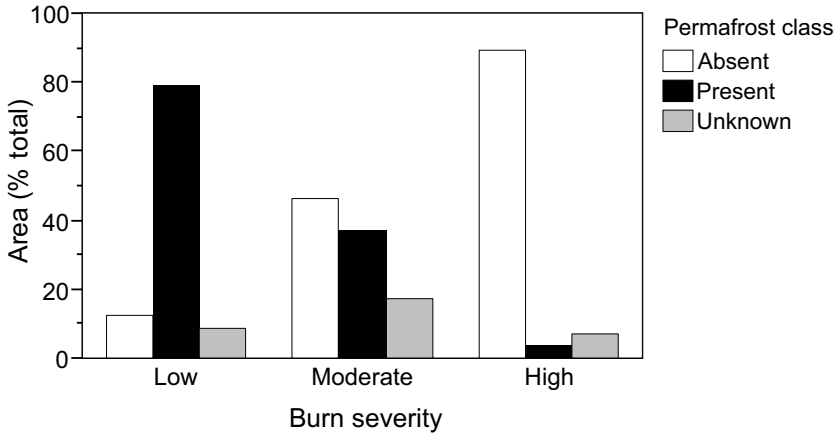

Figure 10. Distribution of mapped permafrost classes by dNBR-derived burn severity (Landsat 7 ETM+).

4. Discussion

4.1. Remote Sensing Indicators of Soil Properties

Of the remote sensing indices considered, we found relationships of ground-based data with elevation and slope from the DEM, with the first principal component of the HV polarization from the ALOS-PALSAR time series, and with multiple indices from Landsat.

We expected to find stronger relationships of soil moisture with the SAR data because microwave sensors measure the dielectric constant of soils, which is directly related to the soil water content [47]. Promising relationships between post-fire soil moisture and SAR backscatter time series have been found elsewhere using the C-band radar signal [41,42]. The greater wavelength of the L-band radar signal of ALOS-PALSAR allows it to more readily penetrate the vegetation canopy and enter deeper into the soil surface. However, in this study there was a several-year time lag between the SAR data acquisition and our field data collection, which may have weakened the strength of the associations. Considering the sensitivity of the radar signal to soil moisture, and the strong relationships between surface moisture and permafrost properties, the use of SAR data has been identified as a high research priority for permafrost mapping [48].

Soil temperature, soil moisture, and plant community composition were related to numerous Landsat-derived indices, including dNBR, NDVI, NDII6, and NDII. dNBR has been used as an indicator of burn severity with inconsistent effectiveness in the boreal forest [49]. We found a weak association of dNBR with organic layer thickness, but strong associations with post-fire soil temperature, moisture, and vegetation composition, site characteristics that are strongly impacted by burn severity. NDVI, a measure of vegetation phytomass or health, was negatively associated with soil temperature, positively associated with soil moisture, and negatively correlated with the primary axis of plant community variation. The inverse relationship between NDVI and dNBR, and the direction of the relationships with soil properties and plant community composition, together suggest that higher NDVI values were due to lower burn severity. Within the early successional environment of this study area, high NDVI values indicated a high proportion of unburned patches or resprouting vegetation typical of low severity burns [35], though in other cases high NDVI values could indicate increases in colonizing vegetation in response to high severity burns. We expect the relationship between NDVI and soil temperature to evolve over time with plant succession. Indeed, an inverse relationship between NDVI and permafrost presence was found at a broad regional scale [28], likely because warm soils tend to support productive vegetation types such as deciduous forests.

The infrared indices (NDII6 and NDII7), which incorporate both the NIR and SWIR bands, were the remote sensing metrics most highly correlated with all measured soil properties and plant communities. Vegetation reflects highly in the NIR region, and water (on the soil surface or within plant leaves) absorbs electromagnetic radiation in the SWIR region. High NIR reflectance and low

SWIR reflectance were indicative of cold soils with high water content. NDII7 was the strongest indicator of surface soil moisture, soil temperature at depth, and organic layer thickness, and was therefore chosen for regression-based spatial modeling of soil properties and more detailed analyses. NDII was also found to be closely related to permafrost presence at the regional scale, presumably because of its sensitivity to water content of vegetation or soils [28]. NDII is sensitive to leaf water content and is commonly considered a vegetation index [50,51], although it is influenced by soils when not obscured by vegetation cover, as is the case after fire disturbance [52]. Therefore, surface soil moisture, which strongly influences SWIR reflectance [53], and vegetation properties are both likely to contribute to NDII in our post-fire study area.

We analyzed seasonal reflectance patterns over several years to determine the extent to which soil moisture versus vegetation properties influenced NDII. Sites with and without near-surface permafrost had the same seasonal patterns of NDII7, NIR, and SWIR reflectance, although reflectance values varied in magnitude. Our interpretation is that the sites with colder soils had greater NIR reflectance due to higher vegetation cover resulting from lower burn severity, and lower SWIR reflectance due to higher water content in plant leaves or the soil surface.

The seasonal surface soil moisture dynamics in this region are driven by spring snowmelt and the seasonal thawing of frozen ground. Surface moisture is typically highest at the time of spring snowmelt and gradually declines through the summer as thaw depth increases [54]. If SWIR were sensitive predominantly to surface soil moisture, we would expect to see SWIR reflectance increase from springtime to fall. Instead, SWIR reflectance decreased from springtime through the summer, and slightly increased in fall. The wide variations in precipitation from 2013–2015, with 2014 a summer of a record-breaking high rainfall, would have influenced surface moisture, yet the seasonal reflectance patterns observed at our field sites were generally consistent each year [55]. The seasonal patterns of NDII7 and NIR reflectance were, however, consistent with expected plant phenology. As vegetation grows and leaves expand from springtime through the summer we see increased NDII7 and NIR reflectance, and subsequent declines in fall as leaves senesce. Across our sites, it therefore appears that the relationship between NDII7 and soil moisture was predominantly an indirect relationship driven by variations in vegetation properties, which reflect burn severity and co-vary with soil properties.

Within severe burns, which have a greater proportion of soil exposure relative to plant cover, direct relationships between SWIR reflectance and surface soil moisture are more likely, however. Our time-series of surface soil moisture from a field monitoring site in a severe burn had a strong negative relationship with SWIR reflectance, suggesting a sensitivity of SWIR reflectance to surface soil moisture. We conclude that NDII7 performed well at predicting subsurface properties because it is an integrative index sensitive both to vegetation properties and surface moisture, both of which are correlated with soil moisture and temperature at depths beyond the reach of optical sensors.

4.2. Controls over Permafrost Distribution and Drainage Class

It has been well documented that the loss of the insulating surface organic layer of soil through wildfire can initiate rapid permafrost degradation [6,56]. The level of degradation is directly related to the thickness of the surface organic layer remaining after disturbance, and thus to burn severity. As expected, an inverse relationship between surface organic layer thickness and soil temperature at 1 m depth was found, demonstrating the positive influence of burn severity over permafrost degradation at our study sites. The strong negative relationship we found between shallow soil moisture (upper 20 cm) and deep temperature (1 m) supports our conjecture that permafrost thawing after fire would result in increased drainage and subsequently drier surface soils in this rocky upland environment [18], since the permafrost table, impermeable to water, strongly controls water table depth, hydrology, and soil moisture regimes [14,20].

Topography also influenced soil properties, as elevation and slope were both positively correlated with soil temperature and negatively with soil moisture. The association of upper slopes with warmer and drier soils and flatter bottomlands with wetter and colder soils is consistent with our understanding

of topographic controls over soil properties [57]. Elevation influences microclimate primarily because of the pronounced wintertime temperature inversions, which cause mean annual air temperatures of lowlands to be significantly lower than adjacent hilltops [6]. Because of the low solar angles at high latitudes, slope and aspect are especially important in mediating solar input, affecting air temperatures, evaporation, and snowmelt [58,59]. Slope further influences the soil environment by controlling the mass flow of water. Mineral soil stratigraphy, soil texture, and loess thickness also tend to co-vary with topography due to differences in material redistribution, typically resulting in thicker deposits of fine-grained soils in lower positions [58,60,61]. The accumulation of thick organic layers in cold and poorly drained landscape positions reinforces cold and wet soil conditions through the development of a shallow permafrost table and through resilience to deep burning and subsequent permafrost degradation [11,31,61,62].

According to our mapping results, 37% of the study area lacked permafrost in the upper meter. Whereas permafrost-free areas occurred on hilltops and upper slopes, they also occurred in lower bottomland landscape positions, where permafrost conditions would be most expected. The inconsistency of topographic controls on permafrost presence suggests that other factors also strongly influence the spatial pattern of permafrost distribution after disturbance. The consistent relationships between burn severity class and mapped permafrost presence provide compelling evidence that burn severity was a key control over the spatial distribution of permafrost. Nearly 90% of the high-severity burn area lacked near-surface permafrost, whereas permafrost persisted across ~80% of the low-severity burn. Some of the deviations from the expected topographic control over permafrost distribution and burn severity could be the result of temporally dynamic factors that influence fire behavior, such as previous precipitation affecting fuel moisture, wind speed/direction, humidity, etc. [62]; or to variation in vegetation and the properties of the surface organic layer, which influence the vulnerability to deep burning [63].

Topography and burn severity both influence the post-fire distribution of permafrost, which in turn impacts soil moisture regimes and landscape hydrology. The prevalent water tracks in our study area are evidence of surface flow due to permafrost. The presence of near-surface permafrost restricts subsurface infiltration, limiting flow to the shallow active layer, and resulting in active layer soils that are wet to saturated [64]. Permafrost-dominated watersheds are thus characterized by flashy near-surface flow, with high peaks of stream discharge responsive to precipitation, and low base flow [65]. As permafrost thaws in a watershed, the water holding capacity of soils increases and flow paths deepen, which cause higher base flow and less responsiveness to precipitation [32].

Burn severity is also tightly linked to vegetation, with the post-fire plant community reflecting the level of disturbance and the pre-fire vegetation [34,66]. Our ordination analysis shows that most of the variation in plant communities occurred along the first axis, which we interpret as a gradient of burn severity due to its close relationships to surface organic layer thickness and dNBR, as well as to patterns of plant species cover. This axis was strongly associated with soil temperature at 1 m depth, and to a lesser extent with surface soil moisture. Low shrub communities were the dominant post-fire vegetation type and encompassed a wide range of permafrost and moisture conditions. Extensive cover of dwarf shrubs (e.g., *Vaccinium vitis-idaea*), low shrubs (e.g., *Rhododendron tomentosum*), sedge tussocks (*Eriophorum vaginatum*), *Sphagnum* spp., and *Rubus chamaemorus* were indicative of low burn severity and colder, wetter soils. Over the broader interior Alaskan region, these particular species have been found to comprise the early successional vegetation of low-severity burns as remnants or resprouts from surviving vegetation, whereas colonizing species regenerating by seed dominate in high severity burns [34,35]. Likewise, we found high cover of grasses and colonizing mosses (e.g., *Ceratodon purpureus*) to be associated with high burn severity and warmer, drier soils. Elevation was positively correlated with the primary axis of plant communities, suggesting a topographic control over burn severity and species composition. Topographic impacts on soil moisture likely interacted with pre-fire vegetation to influence burn severity, creating a range of post-fire early successional communities. These communities were closely related to the infrared remote sensing

indices. The strong associations between post-fire vegetation, soil properties, and remote sensing indices enabled us to indirectly map subsurface properties.

5. Conclusions

With increasing fire extent and severity, there is a growing need for spatial characterization of permafrost within burned areas, particularly within rocky landscapes, which comprise a third of the Alaskan boreal region but for which spatial permafrost data are sparse. Our approach to modeling permafrost status and drainage conditions after fire used the associations among permafrost, soil moisture, and vegetation by establishing empirical relationships between field-based and remotely sensed data. We examined these relationships and landscape-level patterns to identify the possible controls over post-fire permafrost distribution.

We found that burn severity, topography, and vegetation strongly interacted to control permafrost distribution and influence soil moisture after fire. Burn severity influenced the extent of permafrost degradation, which in turn impacted drainage conditions, resulting in drier surface soils. Burn severity also was closely related to plant community composition, which therefore was indicative of these soil conditions. Topography and vegetation also affect the pre-fire soil environment and thus the vulnerability to deep burning.

Because soil temperature at depth was closely linked to post-fire vegetation and surface moisture, remote sensing indices that could capture these surface properties were presumed to perform best as indicators of subsurface permafrost status. Whereas remote sensing indices from all sensors were correlated with measured soil properties, the Landsat-derived infrared index NDII7 was most strongly related to field data. The temporal patterns of NDII7, and its components SWIR and NIR reflectance, suggest that this index was sensitive primarily to vegetation properties linked with burn severity, but also to surface soil moisture in severe burns where soil exposure was less obscured by plant cover.

This study enabled us to model the spatial distribution of permafrost and drainage characteristics after fire by relating satellite data to the surface characteristics of vegetation and soils. Moreover, the analysis of resulting maps allowed us to identify the mechanisms underlying the landscape scale patterns and characterize the ecological and hydrological impacts of fire.

Acknowledgments: This research was funded by the Changing Arctic Ecosystems Initiative of the U.S. Geological Survey's Ecosystem Mission Area and the U.S. Geological Survey's Land Carbon Program, through the Alaska Cooperative Fish and Wildlife Research Unit and the Institute of Arctic Biology at the University of Alaska Fairbanks. We thank Amy Marsh for help with fieldwork, Bruce Wylie for providing the LiDAR data, Rudy Gens for assistance with SAR data processing, Stephanie Ewing and Kimberly Wickland for contributing soil moisture data, and Eugénie Euskirchen, Neal Pastick, Vladimir Romanovsky, and Roger Ruess for insightful reviews of the manuscript. Any use of trade names is for descriptive purposes only and does not imply endorsement by the U.S. Government.

Author Contributions: Dana R.N. Brown and Mark T. Jorgenson conceived and designed the study; Dana R.N. Brown conducted the fieldwork, analyzed the data, and wrote the paper; Mark T. Jorgenson., Knut Kielland, David L. Verbyla, and Anupma Prakash assisted with study design, analysis, and writing; Joshua C. Koch contributed data and editing.

Conflicts of Interest: The authors declare no conflict of interest.

References

1. Osterkamp, T.E.; Romanovsky, V.E. Evidence for warming and thawing of discontinuous permafrost in Alaska. *Permafr. Periglac. Proc.* **1999**, *10*, 17–37. [CrossRef]
2. Jafarov, E.E.; Marchenko, S.S.; Romanovsky, V.E. Numerical modeling of permafrost dynamics in Alaska using a high spatial resolution dataset. *Cryosphere* **2012**, *6*, 613–624. [CrossRef]
3. Zhang, Y.; Chen, W.; Riseborough, D.W. Transient projections of permafrost distribution in Canada uring the 21st century under scenarios of climate change. *Glob. Planet. Chang.* **2008**, *60*, 443–456. [CrossRef]
4. Jorgenson, M.T.; Romanovsky, V.; Harden, J.; Shur, Y.; O'Donnell, J.; Schuur, E.A.G.; Kanevskiy, M.; Marchenko, S. Resilience and vulnerability of permafrost to climate change. *Can. J. For. Res.* **2010**, *40*, 1219–1236. [CrossRef]

5. Johnson, K.D.; Harden, J.W.; David McGuire, A.; Clark, M.; Yuan, F.; Finley, A.O. Permafrost and organic layer interactions over a climate gradient in a discontinuous permafrost zone. *Environ. Res. Lett.* **2013**, *8*, 035028. [CrossRef]
6. Yoshikawa, K.; Bolton, W.R.; Romanovsky, V.E.; Fukuda, M.; Hinzman, L.D. Impacts of wildfire on the permafrost in the boreal forests of interior Alaska. *J. Geophys. Res.* **2003**. [CrossRef]
7. Jafarov, E.E.; Romanovsky, V.E.; Genet, H.; McGuire, A.D.; Marchenko, S.S. The effects of fire on the thermal stability of permafrost in lowland and upland black spruce forests of interior Alaska in a changing climate. *Environ. Res. Lett.* **2013**, *8*, 035030. [CrossRef]
8. Brown, D.R.N.; Jorgenson, M.T.; Douglas, T.A.; Romanovsky, V.E.; Kielland, K.; Hiemstra, C.; Euskirchen, E.S.; Ruess, R.W. Interactive effects of wildfire and climate on permafrost degradation in Alaskan lowland forests. *J. Geophys. Res. Biogeosci.* **2015**, *120*, 1619–1637. [CrossRef]
9. Kasischke, E.S.; Verbyla, D.L.; Rupp, T.S.; McGuire, A.D.; Murphy, K.A.; Jandt, R.; Barnes, J.L.; Hoy, E.E.; Duffy, P.A.; Calef, M.; et al. Alaska's changing fire regime—Implications for the vulnerability of its boreal forests. *Can. J. For. Res.* **2010**, *40*, 1313–1324. [CrossRef]
10. Calef, M.P.; Varvak, A.; McGuire, A.D.; Chapin, F.S.; Reinhold, K.B. Recent changes in annual area burned in interior Alaska: The impact of fire management. *Earth Interact.* **2015**, *19*, 1–17. [CrossRef]
11. Genet, H.; McGuire, A.D.; Barrett, K.; Breen, A.; Euskirchen, E.S.; Johnstone, J.F.; Kasischke, E.S.; Melvin, A.M.; Bennett, A.; Mack, M.C.; et al. Modeling the effects of fire severity and climate warming on active layer thickness and soil carbon storage of black spruce forests across the landscape in interior Alaska. *Environ. Rese. Lett.* **2013**, *8*, 045016. [CrossRef]
12. Schuur, E.A.; McGuire, A.D.; Schadel, C.; Grosse, G.; Harden, J.W.; Hayes, D.J.; Hugelius, G.; Koven, C.D.; Kuhry, P.; Lawrence, D.M.; et al. Climate change and the permafrost carbon feedback. *Nature* **2015**, *520*, 171–179. [CrossRef] [PubMed]
13. Chapin, F.S., III; McGuire, A.D.; Ruess, R.W.; Hollingsworth, T.N.; Mack, M.C.; Johnstone, J.F.; Kasischke, E.S.; Euskirchen, E.S.; Jones, J.B.; Jorgenson, M.T.; et al. Resilience of Alaska's boreal forest to climatic change. *Can. J. For. Res.* **2010**, *40*, 1360–1370. [CrossRef]
14. Woo, M.-K.; Kane, D.L.; Carey, S.K.; Yang, D. Progress in permafrost hydrology in the new millennium. *Permafr. Periglac. Processes* **2008**, *19*, 237–254. [CrossRef]
15. Jorgenson, M.T.; Osterkamp, T.E. Response of boreal ecosystems to varying modes of permafrost degradation. *Can. J. For. Res.* **2005**, *35*, 2100–2111. [CrossRef]
16. Jorgenson, M.T.; Racine, C.H.; Walters, J.C.; Osterkamp, T.E. Permafrost degradation and ecological changes associated with a warming climate in central Alaska. *Clim. Chang.* **2001**, *48*, 551–579. [CrossRef]
17. Koch, J.C.; Ewing, S.A.; Striegl, R.; McKnight, D.M. Rapid runoff via shallow throughflow and deeper preferential flow in a boreal catchment underlain by frozen silt (Alaska, USA). *Hydrogeol. J.* **2013**, *21*, 93–106. [CrossRef]
18. Nossov, D.R.; Jorgenson, M.T.; Kielland, K.; Kanevskiy, M.Z. Edaphic and microclimatic controls over permafrost response to fire in interior Alaska. *Environ. Res. Lett.* **2013**, *8*, 035013. [CrossRef]
19. Koch, J.C.; Kikuchi, C.P.; Wickland, K.P.; Schuster, P. Runoff sources and flow paths in a partially burned, upland boreal catchment underlain by permafrost. *Water Resourc. Res.* **2014**, *50*, 8141–8158. [CrossRef]
20. Jorgenson, M.T.; Harden, J.; Kanevskiy, M.; O'Donnell, J.; Wickland, K.; Ewing, S.; Manies, K.; Zhuang, Q.; Shur, Y.; Striegl, R.; et al. Reorganization of vegetation, hydrology and soil carbon after permafrost degradation across heterogeneous boreal landscapes. *Environ. Res. Lett.* **2013**, *8*, 035017. [CrossRef]
21. Grosse, G.; Harden, J.; Turetsky, M.; McGuire, A.D.; Camill, P.; Tarnocai, C.; Frolking, S.; Schuur, E.A.G.; Jorgenson, T.; Marchenko, S.; et al. Vulnerability of high-latitude soil organic carbon in North America to disturbance. *J. Geophys. Res.* **2011**, *116*, G00K06. [CrossRef]
22. Minsley, B.J.; Abraham, J.D.; Smith, B.D.; Cannia, J.C.; Voss, C.I.; Jorgenson, M.T.; Walvoord, M.A.; Wylie, B.K.; Anderson, L.; Ball, L.B.; et al. Airborne electromagnetic imaging of discontinuous permafrost. *Geophys. Res. Lett.* **2012**, *39*. [CrossRef]
23. Hachem, S.; Allard, M.; Duguay, C. Using the modis land surface temperature product for mapping permafrost: An application to northern Quebec and Labrador, Canada. *Permafr. Periglac. Proc.* **2009**, *20*, 407–416. [CrossRef]
24. Langer, M.; Westermann, S.; Heikenfeld, M.; Dorn, W.; Boike, J. Satellite-based modeling of permafrost temperatures in a tundra lowland landscape. *Remote Sens. Environ.* **2013**, *135*, 12–24. [CrossRef]

25. Westermann, S.; Østby, T.I.; Gisnås, K.; Schuler, T.V.; Etzelmüller, B. A ground temperature map of the North Atlantic permafrost region based on remote sensing and reanalysis data. *Cryosphere* **2015**, *9*, 1303–1319. [CrossRef]
26. Nelson, F.E.; Shiklomanov, N.; Mueller, G.R.; Hinkel, K.M.; Walker, D.A.; Bockheim, J.G. Estimating active-layer thickness over a large region: Kuparuk River Basin, Alaska, U.S.A. *Arctic Alpine Res.* **1997**, *29*, 367–378. [CrossRef]
27. Panda, S.K.; Prakash, A.; Solie, D.N.; Romanovsky, V.E.; Jorgenson, M.T. Remote sensing and field-based mapping of permafrost distribution along the Alaska Highway corridor, interior Alaska. *Permafr. Periglac. Proc.* **2010**, *21*, 271–281. [CrossRef]
28. Pastick, N.J.; Jorgenson, M.T.; Wylie, B.K.; Nield, S.J.; Johnson, K.D.; Finley, A.O. Distribution of near-surface permafrost in Alaska: Estimates of present and future conditions. *Remote Sens. Environ.* **2015**, *168*, 301–315. [CrossRef]
29. Karlstrom, T.N.V. *Surficial Geology of Alaska*; IMAP, U.S. Geological Survey: Richmond, VA, USA, 1994.
30. Jorgenson, M.T.; Yoshikawa, K.; Kanevskiy, M.; Shur, Y.; Romanovsky, V.; Marchenko, S.; Grosse, G.; Brown, J.; Jones, B. *Permafrost Characteristics of Alaska*; Institute of Northern Engineering, University of Alaska Fairbanks: Fairbanks, AK, USA, 2008.
31. Swanson, D.K. Susceptibility of permafrost soils to deep thaw after forest fires in interior Alaska, U.S.A., and some ecologic implications. *Arctic Alp. Res.* **1996**, *28*, 217–227. [CrossRef]
32. Jones, J.B.; Rinehart, A.J. The long-term response of stream flow to climatic warming in headwater streams of interior Alaska. *Can. J. For. Res.* **2010**, *40*, 1210–1218. [CrossRef]
33. Alaska Climate Research Center. Climate Normals from the 30-year Time Period from 1981–2010, Provided by the National Climatic Data Center. Available online: http://climate.Gi.Alaska.Edu/climate/normals (accessed on 12 May 2014).
34. Bernhardt, E.L.; Hollingsworth, T.N.; Chapin, F.S., III. Fire severity mediates climate-driven shifts in understorey community composition of black spruce stands of interior Alaska. *J. Veg. Sci.* **2011**, *22*, 32–44. [CrossRef]
35. Hollingsworth, T.N.; Johnstone, J.F.; Bernhardt, E.L.; Chapin, F.S. Fire severity filters regeneration traits to shape community assembly in Alaska's boreal forest. *PLoS ONE* **2013**, *8*, e56033.
36. Minsley, B.J.; Pastick, N.J.; Wylie, B.K.; Brown, D.R.N.; Kass, M.A. Evidence for nonuniform permafrost degradation after fire in boreal landscapes. *J. Geophys. Res. Earth Sur.* **2016**, *121*, 320–335. [CrossRef]
37. Viereck, L.A.D.C.T.; Batten, A.R.; Wenzlick, K.J. *The Alaska Vegetation Classification. General Technical Report Pnw-gtr-286*; U.S. Department of Agriculture, Forest Service, Pacific Northwest Research Station: Portland, OR, USA, 1992.
38. Braun-Blanquet, J. *Plant Sociology: The Study of Plant Communities*; Hafner: London, UK, 1965.
39. Rich, P.M.; Dubayah, R.; Hetrick, W.A.; Saving, S.C. Using viewshed models to calculate intercepted solar radiation: Applications in ecology. *Am. Soc. Photogramm. Remote Sens.* **1994**, *1994*, 524–529.
40. Moore, I.D.; Grayson, R.B.; Ladson, A.R. Digital terrain modelling: A review of hydrological, geomorphological, and biological applications. *Hydrol. Proc.* **1991**, *5*, 3–30. [CrossRef]
41. Bourgeau-Chavez, L.L.; Kasischke, E.S.; Riordan, K.; Brunzell, S.; Nolan, M.; Hyer, E.; Slawski, J.; Medvecz, M.; Walters, T.; Ames, S. Remote monitoring of spatial and temporal surface soil moisture in fire disturbed boreal forest ecosystems with ERS SAR imagery. *Int. J. Remote Sens.* **2007**, *28*, 2133–2162. [CrossRef]
42. Kasischke, E.S.; Bourgeau-Chavez, L.L.; Johnstone, J.F. Assessing spatial and temporal variations in surface soil moisture in fire-disturbed black spruce forests in interior Alaska using spaceborne synthetic aperture radar imagery—Implications for post-fire tree recruitment. *Remote Sens. Environ.* **2007**, *108*, 42–58. [CrossRef]
43. U.S. Geological Survey, Department of the Interior. *Product Guide: Provisional Landsat 8 Surface Reflectance Code (LaSRC) Product*; Version 3. U.S. Geological Survey: Sioux Falls, SD, USA, 2016.
44. Vermote, E.; Justice, C.; Claverie, M.; Franch, B. Preliminary analysis of the performance of the Landsat 8/OLI land surface reflectance product. *Remote Sens. Environ.* **2016**. [CrossRef]
45. McCune, B.; Grace, J.B. *Analysis of Ecological Communities*; MjM Software Design: Gleneden Beach, OR, USA, 2002.
46. Jenks, G.F. The data model concept in statistical mapping. *Int. Yearbook Cartogr.* **1967**, *7*, 186–190.
47. Kerr, Y.H. Soil moisture from space: Where are we? *Hydrogeol. J.* **2006**, *15*, 117–120. [CrossRef]

48. National Research Council. *Opportunities to Use Remote Sensing in Understanding Permafrost and Related Ecological Characteristics: Report of a Workshop*; National Academies Press: Washington, DC, USA, 2014.
49. French, N.H.F.; Kasischke, E.S.; Hall, R.J.; Murphy, K.A.; Verbyla, D.L.; Hoy, E.E.; Allen, J.L. Using Landsat data to assess fire and burn severity in the North American boreal forest region: An overview and summary of results. *Int. J. Wildland Fire* **2008**, *17*, 443–462. [CrossRef]
50. Kimes, D.S.; Markham, B.L.; Tucker, C.J.; McMurtrey, J.E., III. Temporal relationships between spectral response and agronomic variables of a corn canopy. *Remote Sens. Environ.* **1981**, *11*, 401–411. [CrossRef]
51. Ji, L.; Zhang, L.; Wylie, B.K.; Rover, J. On the terminology of the spectral vegetation index (NIR − SWIR)/(NIR + SWIR). *Int. J. Remote Sens.* **2011**, *32*, 6901–6909. [CrossRef]
52. Wang, L.; Qu, J.J. NMDI: A normalized multi-band drought index for monitoring soil and vegetation moisture with satellite remote sensing. *Geophys. Res. Lett.* **2007**, *34*. [CrossRef]
53. Weidong, L.; Baret, F.; Xingfa, G.; Qingxi, T.; Lanfen, Z.; Bing, Z. Relating soil surface moisture to reflectance. *Remote Sens. Environ.* **2002**, *81*, 238–246. [CrossRef]
54. Romanovsky, V.E. Bonanza Creek 2—Burned: Soils, Geophysical Institute Permafrost Laboratory, University of Alaska Fairbanks. Available online: http://lapland.Gi.Alaska.Edu/vdv/index.Html (accessed on 28 July 2016).
55. Alaska Climate Research Center. Acis Daily Data Browser. 2016; Volume 2016. Available online: http://climate.Gi.Alaska.Edu/acis_data (accessed on 25 March 2016).
56. Viereck, L.A. Effects of fire and firelines on active layer thickness and soil temperatures in Interior Alaska. *Perma. Soils* **1982**, *1982*, 123–134.
57. Van Cleve, K.; Chapin, F.S., III; Flanagan, P.W.; Viereck, L.A.; Dyrness, C.T. *Forest Ecosystems in the Alaskan Taiga: A synthesis of Structure and Function*; Springer-Verlag: New York, NY, USA, 1986.
58. Péwé, T.L. *Quaternary Geology of Alaska*; United States Geological Survey: Washington, DC, USA, 1975.
59. Hinzman, L.D.; Viereck, L.A.; Adams, P.C.; Romanovsky, V.E.; Yoshikawa, K. Climate and permafrost dynamics of the Alaskan boreal forest. In *Alaska's Changing Boreal Forest*; Chapin, F.S., III, Oswood, M.W., Van Cleve, K., Viereck, L.A., Verbyla, D.L., Eds.; Oxford University Press: New York, NY, USA, 2006.
60. Rieger, S.; DeMent, J.A.; Sanders, D. *Soil Survey of Fairbanks Area, Alaska. USDA Soil Conservation Service*; U.S. Government Printing Office: Washington, DC, USA, 1963.
61. Ping, C.L.; Michaelson, G.J.; Packee, E.C.; Stiles, C.A.; Swanson, D.K.; Yoshikawa, K. Soil catena sequences and fire ecology in the boreal forest of Alaska. *Soil Sci. Soc. Am. J.* **2005**, *69*, 1761. [CrossRef]
62. Barrett, K.; Kasischke, E.S.; McGuire, A.D.; Turetsky, M.R.; Kane, E.S. Modeling fire severity in black spruce stands in the Alaskan boreal forest using spectral and non- spectral geospatial data. *Remote Sens. Environ.* **2010**, *114*, 1494–1503. [CrossRef]
63. Kane, E.S.; Kasischke, E.S.; Valentine, D.W.; Turetsky, M.R.; McGuire, A.D. Topographic influences on wildfire consumption of soil organic carbon in interior Alaska: Implications for black carbon accumulation. *J. Geophys. Res.* **2007**, *112*. [CrossRef]
64. Hinzman, L.D.; Bolton, W.R.; Petrone, K.C.; Jones, J.B.; Adams, P.C. Watershed hydrology and chemistry in the Alaskan boreal forest: The central role of permafrost. In *Alaska's Changing Boreal Forest*; Chapin, F.S., III, Oswood, M.W., Van Cleve, K., Viereck, L.A., Verbyla, D., Eds.; Oxford University Press: New York, NY, USA, 2006; pp. 269–284.
65. Bolton, W.R.; Hinzman, L.; Yoshikawa, K. *Stream Flow Studies in a Watershed Underlain by Discontinuous Permafrost*; American Water Resources Association: Anchorage, AK, USA, 2000.
66. Shenoy, A.; Johnstone, J.F.; Kasischke, E.S.; Kielland, K. Persistent effects of fire severity on early successional forests in interior Alaska. *For. Ecol. Manag.* **2011**, *261*, 381–390. [CrossRef]